Preprint

Guo, L., Latham, J.-P., Xiang, J., 2017. A numerical study of fracture spacing and through-going fracture formation in layered rocks. International Journal of Solids and Structures 110-111, 44-57.

http://dx.doi.org/10.1016/j.ijsolstr.2017.02.004

A numerical study of fracture spacing and through-going fracture formation in layered rocks

Liwei Guo[1,*], John-Paul Latham and Jiansheng Xiang

Department of Earth Science and Engineering, Imperial College London, South Kensington Campus, London SW7 2AZ, United Kingdom

E-mail address: liwei.guo@ucl.ac.uk (Liwei Guo), j.p.latham@imperial.ac.uk (John-Paul Latham), j.xiang@imperial.ac.uk (Jiansheng Xiang).

Abstract

Naturally fractured reservoirs are an important source of hydrocarbons. Computational models capable of generating fracture geometries according to geomechanical principles offer a means to create a numerical representation of a more realistic rock mass structure. In this work, the combined finite-discrete element method is applied to investigate fracture patterns in layered rocks. First, a three-layer model undergoing layer normal compression is simulated with the aim of examining the controls on fracture spacing in layered rocks. Second, a seven-layer model with low competence contrast is modelled under direct tension parallel to the layering and bending conditions with the focus on investigating through-going fracture formation across layer interfaces. The numerical results give an insight into the understanding of various mechanisms that contribute to fracture pattern development in layered rocks.

Keywords: numerical study, fracture model, combined finite-discrete element method, layered rocks, fracture spacing, through-going fracture

* Corresponding author. Tel.: +44 (0)20 3108 9514.
E-mail address: liwei.guo@ucl.ac.uk (Liwei Guo).
[1] Present address: Department of Mechanical Engineering, University College London, Torrington Place, London WC1E 7JE, United Kingdom.

1 Introduction

Naturally fractured reservoirs around the world are an important source of hydrocarbons. The difficulty in characterising such reservoirs is mainly attributed to the lack of sufficient sub-surface data to create realistic fracture network models (Nelson, 2001). The first fracture network models simulated by Priest and Hudson (1976) provided a basis for the development of Discrete Fracture Networks (DFNs), which are now widely used to estimate permeability in reservoir engineering (e.g. Min et al., 2004). Although DFNs have brought many benefits to reservoir engineers, they lack certain mechanically realistic fracture relations, such as cross-cutting, branching, and truncation; these relations, however, have a significant impact on the bulk flow and geomechanical properties of a reservoir. Understanding mechanisms and processes of fracture pattern formation can help to predict fracture characteristics in different stress regimes. One study area of great importance is the research of fracture development in relation to layered rocks to understand the role of fractures in vertical fluid migration across and within sedimentary rock layers (Bai et al., 2000b; Becker and Gross, 1996; Doolin and Mauldon, 2001; Helgeson and Aydin, 1991).

A considerable amount of literature exists on the geological setting and stress regimes in sedimentary rock that generate brittle and ductile structures as a consequence. A good discussion of the mechanical principles and concepts used to analyse geological structures including those mentioned below can be found in the book by Price and Cosgrove (1990). Sedimentary sequences in reservoir basins at different stages in their geological evolution to the present day may have been exposed to phases of deformation involving both layer extension and layer compression. Research on layered rock (Wu and Pollard, 1995) concluded that opening-mode tensile fractures are a common occurrence, and these are often confined and terminated by layer boundaries. However, sometimes through-going fractures are observed which penetrate many layer boundaries (Finn et al., 2003; Gross and Eyal, 2007). The mechanisms allowing this significant pathway for fluids to develop are not well understood and are the subject of great interest to structural geologists and reservoir engineers concerned with the integrity of cap rock.

In this work the focus is on the formation of tensile fractures in layered rocks. Such multi-layer systems appear to have been subjected to direct layer parallel tensile stresses. Although intuition might suggest all three principal stresses in the ground

will be compressive ($\sigma_1 < 0$, $\sigma_2 < 0$, and $\sigma_3 < 0$; it should be noted that the engineering mechanics sign convention is used in this paper, which means tensile stress is positive and compressive stress is negative), there is a range of circumstances in which this is not so and tensile stresses initiate geological structures. One example is a half-graben basin overlying a major listric, i.e. upward steepening fault (Fossen, 2010; Schlische, 1991). In such basins a roll-over anticline forms in the downward warping upper sequence, where direct tensile stresses build up in the multilayer sequence, as it is forced to stretch and fill the missing space. Another is the stretching of a sequence overlying an ascending diaper, e.g. a salt dome structure (Schultz-Ela et al., 1993). Also, a very common occurrence even to considerable depths in a reservoir is where, e.g. due to rapid sediment burial, the elevated fluid pressures may exceed the value of the applied maximum principal stress σ_1. Therefore, the maximum effective principal stress, i.e. accounting for pore fluid pressure and governing tensile failure, is in many respects equivalent to a direct tension.

Whereas buckle folds are associated with layer parallel compression, forced folds develop by boundary deflections at high angles to the bedding and are more readily acknowledged as facilitating stretching. There are, however, interesting analogies between forced folds and unstratified buckle folds. Two end member models for the deformation within layers folded by buckling are Tangential Longitudinal Strain (TLS) and Flexural Flow (FF) (Ramsay, 1967). Tangential Longitudinal Strain (TLS) is deformation response where the material behaves isotropically; the outer-arc stretches, and the inner-arc compresses, and the neutral surface, which will move during fold amplification, separates the material being extended parallel to the compression direction from that which is being shortened. Flexural Flow (FF) is a deformation field that would be associated with a transversely anisotropic behaviour allowing easy shear parallel to the layering. When interface slip is activated as a dominant deformation mechanism in fold amplification, the term flexural slip is used.

These various settings that are known to initiate tensile fractures perpendicular to layer boundaries, namely direct layer parallel extension and forced folding, have informed the choice of boundary conditions that have been applied to the layered models in this research. A few numerical modelling studies have also been attracted by this problem. Bai and Pollard (2000a) simulated an elastic three-layer model, where vertical fractures were inserted in the central layer as pre-existing fractures. Tang et al. (2008) modelled the entire fracture evolution until saturation using a

strain-dependent finite element based degradation model. The work of Bai and Pollard (2000a) and Tang et al. (2008) used two-dimensional models with the boundary condition in which only tensile stress directed parallel to the associated layers was applied. Discussion of the fracture evolution caused by layer normal compressive stress in layered rock, e.g. induced by overburden or burial, was outside the scope of their papers. Both of their studies assumed that the two materials across the layer boundaries were initially welded together, i.e. no slip or opening was permitted along the boundary. Interestingly, Tang et al. (2008) were able to show that delamination was almost certainly occurring in their simulations. Here delamination means the two sides of an interface between two adjacent layers have relative displacement. Slip between beds and on curved sections of otherwise planar faults contributes to pull-apart structures and thus slip between opposite sides of an interface cannot be considered negligible. A better solution to numerical modelling of layered rocks is to introduce discrete surfaces as layer interfaces and use contact mechanics to simulate the interaction of neighbouring layers at interfaces.

The objective of this paper is to investigate fracture spacing and through-going fracture formation in layered rocks by two-dimensional numerical simulations using the combined finite-discrete element method. The main novelty of using this numerical method is that layer interfaces can be explicitly represented by discrete surfaces with frictional properties and governed by contact mechanics laws, which is essential for accurate understanding of this problem but has been missing in previous research. The numerical study in this paper includes two parts. The first part focuses on examining the controls on fracture spacing to layer thickness ratio in a three-layer shale-limestone-shale sequence undergoing layer normal compression. The second part models through-going fracture formation in a seven-layer limestone sequence subject to direct tension and bending conditions with the focus on the fracturing behaviour across layer interfaces. As a non-traditional numerical method is used for this research, a brief introduction and two verification examples of the method are given before presenting the numerical results of layered-rocks.

2 Numerical method

Numerical methods provide important tools for the research of fracturing behaviour in quasi-brittle materials, e.g. rock, concrete, ceramics, etc. Many models have been

developed in the field of computational fracture mechanics, such as linear and non-linear elastic fracture mechanics based methods (Bittencourt et al., 1996; Ingraffea and Manu, 1980; Swenson and Ingraffea, 1988), the extended finite element method (XFEM) (Belytschko and Black, 1999; Karihaloo and Xiao, 2003; Melenk and Babuška, 1996; Sukumar and Prévost, 2003), the cohesive-zone model (Bocca et al., 1991; de Borst, 2003) and meshless methods, such as the element free Galerkin method (EFGM) (Bordas et al., 2008; Fleming et al., 1997). Moreover, discontinuum-based numerical methods that are originally used for granular materials, such as the smoothed particle hydrodynamics (SPH) method (Das and Cleary, 2010; Gray et al., 2001; Ma et al., 2011) and the discrete element method (DEM) (Cundall and Strack, 1979; Morris et al., 2004; Shi and Goodman, 1985) have also become increasingly popular in fracture modelling. In actual numerical simulations of engineering applications, the choice of modelling approach should be based on the likely failure mechanism of the material, i.e. whether it is a failure of material, discontinuity or a combination of both (Coggan et al., 2014).

The numerical method used in this paper is the combined finite-discrete element method (FEMDEM) (Munjiza, 2004). The reason to choose this method is that it is capable of modelling mechanical behaviour both in the continuum domain (e.g. deformation and stress distribution) and across discontinuities (e.g. interaction between discrete layer interfaces). In this method, the whole domain is discretised by both discrete element meshes and finite element meshes. For example, in a layered system, each layer is a discrete element, and inside each layer there is a finite element mesh associated with it; in a two-dimensional domain, 3-node triangular elements are used for the finite element mesh. The transition from continuum to discontinuum, which gives an explicit geometric realisation of fracture patterns, is modelled through fracturing and fragmentation processes and controlled by a failure criterion. An explicit time integration scheme is used to calculate the deformed configuration. In the numerical results presented in this paper, the loading is slow enough so that dynamic effects can be neglected. The details of the FEMDEM method and its fracture model can be found elsewhere (Guo, 2014; Munjiza, 2004; Xiang et al., 2009) and here only some key aspects are briefly introduced.

2.1 Pre-failure

Before fractures initiating from stress concentrations or propagating from pre-existing crack tips, the domain is in a state of continuum deformation under external loading. The algorithms of stress calculation are implemented in a standard finite element formulation. The constitutive model used for 3-node triangular elements is a neo-Hookean viscoelastic material model (Bonet and Wood, 1997), so the Cauchy stress tensor **T** can be calculated as

$$\mathbf{T} = \frac{\mu}{J}\left(\mathbf{B} - \mathbf{I}\right) + \frac{\lambda}{J}\left(\ln J\right)\mathbf{I} + \eta\mathbf{D} \tag{1}$$

where μ and λ are Lamé constants, **B** is the Left Cauchy-Green strain tensor, J is the determinant of the deformation gradient matrix **F**, η is the viscous parameter, and **D** is the rate of deformation, which is calculated from the velocity gradient **L** and is symmetric (Munjiza, 2004).

$$\mathbf{D} = \frac{1}{2}\left(\mathbf{L} + \mathbf{L}^{\mathrm{T}}\right) \tag{2}$$

2.2 Failure criterion

The failure criterion is applied to the interface elements, which are inserted between triangular elements. When the failure criterion is satisfied the local interface element will break, so the adjacent triangular elements will be physically separated and the interaction of the separated element edges (normal compression and sliding friction, see section 2.3) can model the realistic scenarios of contact between discrete fracture walls.

When fractures initiate or propagate, the assumption here is that there exists a plastic zone corresponding to a micro-fractured zone with some remaining ligaments for stress transfer in front of the actual fracture tip (Hillerborg et al., 1976, Figure 1). The stresses in the plastic zone are calculated by a constitutive relation called the combined single and smeared crack model (Munjiza et al., 1999), which is based on the accurate representation of the stress-stain relation in direct tension, and includes a strain softening part to characterise the deterioration of material strength (Figure 2). Therefore, the normal stress σ in interface elements can be calculated following the stress-displacement relation in Figure 2,

$$\sigma = \begin{cases} 2\dfrac{\delta_n}{\delta_{np}} f_t, & \text{if } \delta_n < 0 \\ \left[2\dfrac{\delta_n}{\delta_{np}} - \left(\dfrac{\delta_n}{\delta_{np}} \right)^2 \right] f_t, & \text{if } 0 \le \delta_n \le \delta_{np} \\ z f_t, & \text{if } \delta_{np} < \delta_n \le \delta_{nc} \end{cases} \tag{3}$$

where f_t is the tensile strength, δ_n is the relative displacement in the normal direction in the interface element, δ_{np} is the maximum elastic displacement, δ_{nc} is the critical displacement at failure, z is a heuristic softening parameter obtained by curve fitting using experiment data (Munjiza et al., 1999; Xian et al., 1991). In a similar way, the shear stress τ can be calculated by substituting normal displacement δ_n with shear displacement δ_s, and other parameters in the normal direction (with subscript n) with the corresponding parameters in the shear direction (with subscript s).

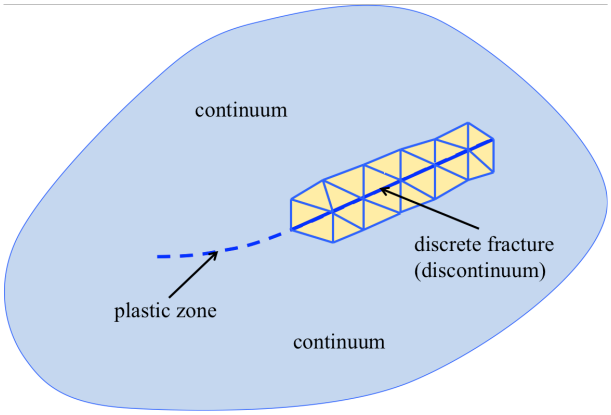

Figure 1: Schematic illustration of the transition from continuum to discontinuum. The yellow area shows the contacting couples at both sides of the discrete fracture.

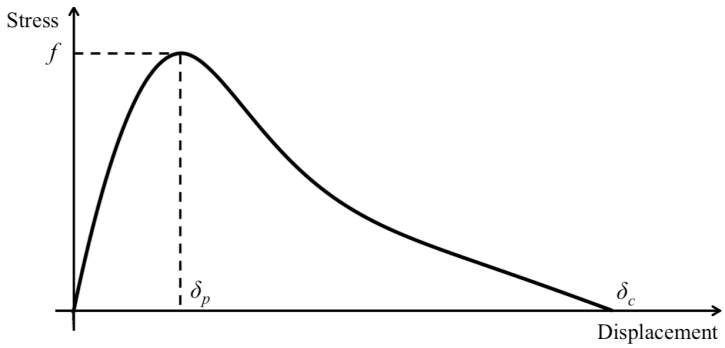

Figure 2: The constitutive relation for interface elements.

The failure criterion used here is the Mohr-Coulomb criterion with a tension cut-off, which defines the strength parameter f in Figure 2. It assumes the tensile strength f_t is a constant and defines the shear strength f_s as

$$f_s = c - \sigma_n \tan\phi \tag{4}$$

where c is the cohesion, ϕ is the internal friction angle, and σ_n is the normal stress acting perpendicular to the shear direction. It should be noted that because the normal stress σ_n cannot exceed the tensile strength f_t, the tension cut-off that happens when $\sigma_n \geq f_t$ is automatically guaranteed in Equation 4. Based on the material strengths defined by the Mohr-Coulomb criterion, the interface elements will fail when the relative displacement reaches its critical value δ_c (Figure 1), which is defined by the Griffith theory (1921). It assumes that a certain amount of energy is absorbed by the formation of a unit area of the fracture surface in a brittle medium, which is called the fracture energy G_f and it is a material property. Therefore, the formation of fractures will cause the system energy to decrease. In terms of fracture coalescence (e.g. several fractures grow in the domain), the one whose stress at its tip satisfies the failure criterion first will grow first. Because the failure criterion is locally defined at material points, so all scenarios of fracture formation, including initiation, growth and coalescence, etc., are all treated as material failure at the discretised element level. Although this concept is a simplification of the complicated problem, and is different from the variational model based on energy minimisation (Francfort and Marigo, 1998), it has a similar effect of minimising the elastic potential energy in the domain. It should be noted that because interface elements are only inserted between triangular elements, fractures could only propagate along element boundaries. However, although the fracture pattern is locally mesh-dependent, from a global point of view its influence is insignificant if the element size is small enough, i.e. only a fraction of the length of the process zone in front of the fracture tip (Guo et al., 2016; Munjiza and John, 2002).

2.3 Post-failure

After interface elements fail, discrete fractures will form between triangular elements. Numerically, the formation of fractures means the transition of algorithms to calculate the constraints between triangular elements. Before fracture formation, the adjacent triangular elements are constrained by interface elements. When the local stress in the interface element reaches the material strength, and eventually drops to zero after the

softening stage, a fracture will form. After fracture formation, the constitutive relation defined in Figure 2 becomes inoperative on the failed interface element. Instead, discrete fragment motion and interaction across discrete fracture walls during progressive deformation are tracked by contact laws implemented in the discrete element formulation, which are also used to simulate the frictional behaviour. The triangular mesh is fixed and does not change during the simulation, e.g. no addition or deletion of elements or nodes. The contact algorithms used in the FEMDEM method include two parts: contact detection and contact interaction. The contact detection is performed by an NBS (no binary search) contact detection algorithm (Munjiza and Andrews, 1998). The algorithm for contact interaction (Munjiza and Andrews, 2000) is based on the penalty function method and incorporating contact kinematics preserving energy balance. In this algorithm, penetration between discrete elements will generate a pair of contact forces, which are equal and opposite acting on the two triangular elements of a contacting couple (yellow area in Figure 1). The two triangular elements of a contacting couple are named contactor and target, respectively. The contact force $\mathbf{f}_{contact}$ generated due to penetration is then calculated as

$$\mathbf{f}_{contact} = \sum_{i=1}^{m}\sum_{j=1}^{n}\int_{A_{ij}=\beta_{ci}\cap\beta_{tj}}\left(grad\varphi_{ci} - grad\varphi_{tj}\right)dA_{ij} \tag{5}$$

where dA_{ij} is an infinitesimal overlap between contactor element β_{ci} and target element β_{tj}, m and n are the total number of triangular elements into which the contactor and target discrete elements are discretised, φ_{ci} and φ_{tj} are potential functions for the contactor element β_{ci} and the target element β_{tj}, respectively.

Sliding friction is also considered as a type of contact and a Coulomb friction law is implemented into the numerical code. Sliding in the tangential direction at the contact interface will occur when the tangential contact force f_{tan} is greater than μN, where μ is the friction coefficient, and N is the normal pressure at the contact interface. It should be noted that the microscopic roughness of fracture surfaces is not considered here.

3 Verification of the numerical method

In this section, numerical experiments are conducted to verify the numerical models used for the simulations of layered-rocks. Two aspects in the FEMDEM method that

are most relevant to the mechanical behaviour in layered-rocks are verified here: one is the Mohr-Coulomb failure criterion, which controls the formation of fractures; the other one is the Coulomb friction law, which governs the frictional interaction between discrete layer interfaces as well as fracture walls. Thorough convergence studies of the numerical model used in this paper can be found in the papers from Munjiza et al. (1995, 1999) and Munjiza and John (2002), and more verification and validation cases can be found elsewhere (Farsi et al., 2015; Wang, 2010).

3.1 Mohr-Coulomb failure criterion

The Mohr-Coulomb criterion with a tension cut-off has been implemented to define shear strength as a function of mean stress (Equation 4). A numerical test is set up to verify the fracture patterns formed under biaxial compressive loading conditions (Figure 3). The upper loading platen moves vertically downwards at a constant velocity 0.1 m/s and the lower platen is fixed. A confining pressure of 5 MPa is applied to the left and right sides of the specimen, which has the material properties as follows: density ρ = 2700 kg·m^{-3}, Young's modulus E = 60 GPa, Poisson's ratio υ = 0.35, tensile strength f_t = 5 MPa, cohesion c = 12 MPa.

Four internal friction angles ϕ = 20°, 30°, 40°, 50° are tested in the modelling. Depending on different internal friction angles, the computational time (serial computation) of each test varies between 10 h and 17 h. According to the Mohr-Coulomb theory, the conjugate slip planes should have angles of 45° ± ϕ/2 with the direction of the minimum compressive stress (horizontal direction). It can be seen from Figure 4 that the fracture patterns obtained from numerical modelling fit well with the theoretical predictions (red dashed lines). It should be noted that there are no pre-existing flaws or weaknesses in the specimen before the loading starts, so the initiation of the first fracture is to a large extent affected by numerical perturbation, but after that the overall fracture patterns are formed by mechanical principles. It is also worth noting that although the geometry and loading conditions are symmetric, because the mesh is irregular (Figure 3) and fractures can only develop along element boundaries, the fracture patterns are asymmetric.

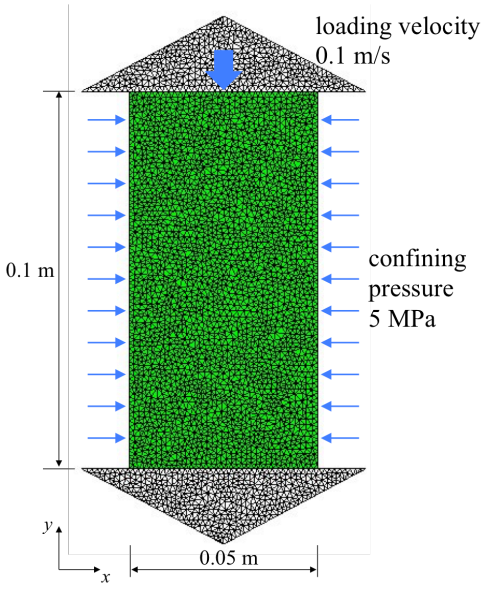

Figure 3: Test setup for the Mohr-Coulomb failure criterion.

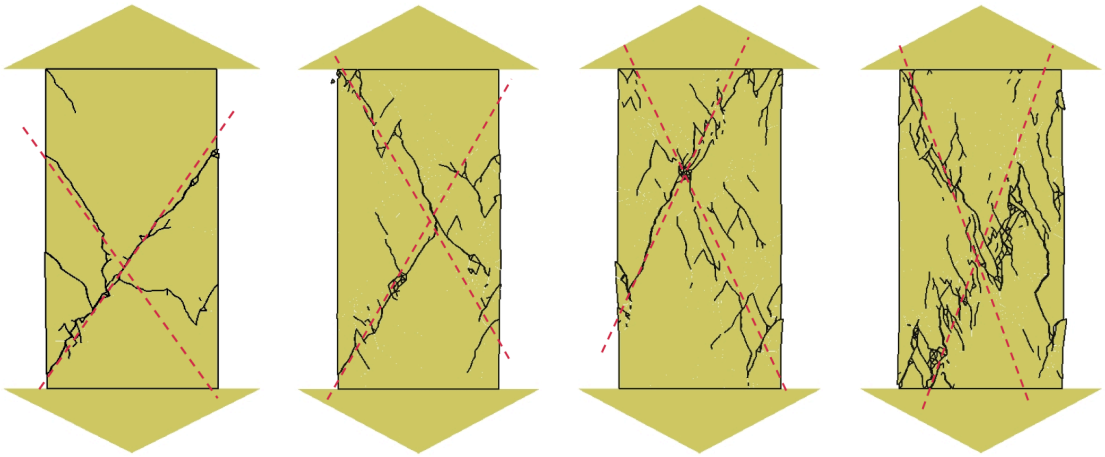

Figure 4: Numerical results of fracture patterns for different internal friction angles. The red dashed lines show the theoretical conjugate slip planes.

3.2 Coulomb friction law

A Coulomb friction law has been implemented in the numerical code to model sliding friction between layers and discrete fracture surfaces. A benchmark test is simulated with different friction coefficients. The setup of the benchmark test is a square block with an initial horizontal velocity v_{xi} sliding on a fixed horizontal base (Figure 5a). Due to the friction between the square and the base, the square will stop at a certain distance, which is called the stop distance L and can be calculated analytically by

$$L = \frac{v_{xi}^2}{2\mu g} \tag{6}$$

where g is the acceleration of gravity, g = 9.8 m/s^2. Three different friction coefficients μ = 0.1, 0.5 and 1.0, and six different initial horizontal velocities v_{xi} = 0, 1, 2, 3, 4, and 5 m/s are tested in the numerical simulations. The numerical results for initial horizontal velocity v_{xi} = 5 m/s are shown in Figure 5, and all of the numerical results are plotted with theoretical solutions in Figure 6. It can be seen that the numerical results are in good agreement with theoretical solutions calculated by Equation 6 for all the friction coefficients and initial horizontal velocities being tested.

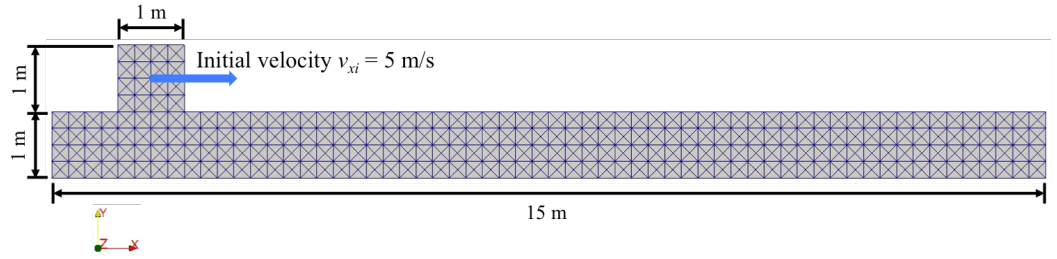

a. Test setup.

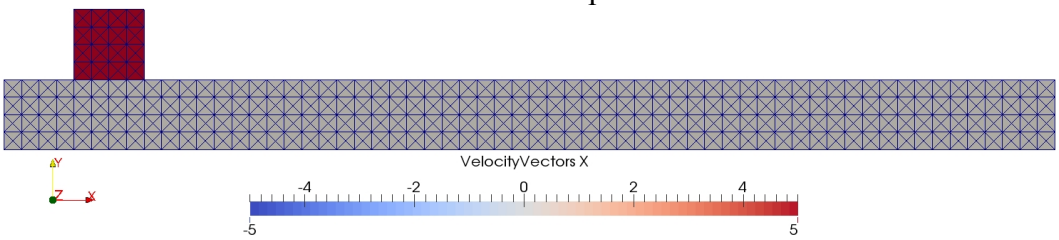

b. Initial state.

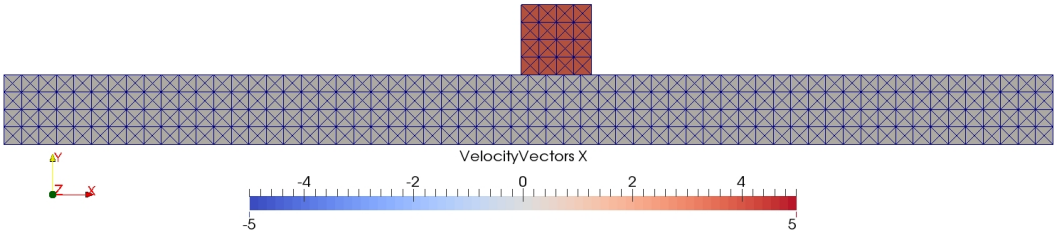

c. Transient state.

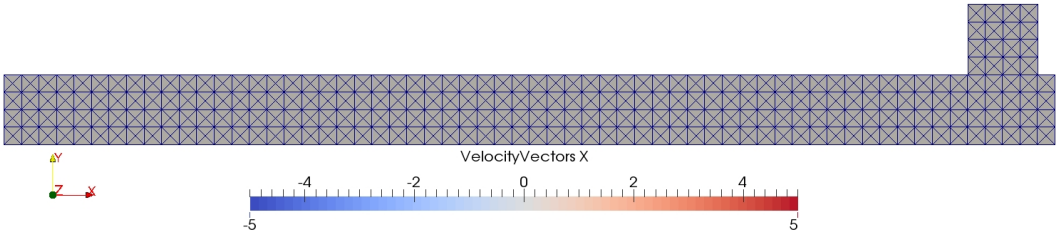

d. Final state.

Figure 5: Benchmark test setup for the Coulomb friction law and numerical results for initial horizontal velocity v_{xi} = 5 m/s.

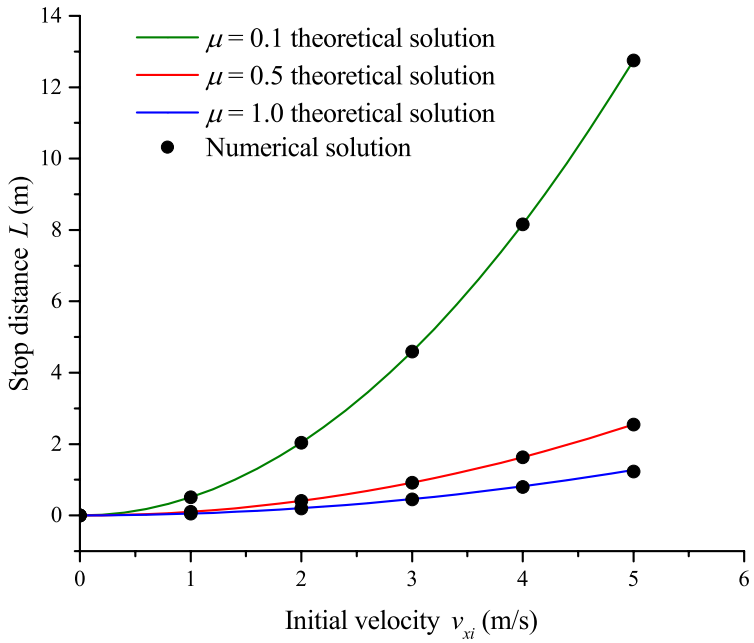

Figure 6: Comparison between numerical results and theoretical solutions.

4 Investigation of tensile fracture spacing under layer normal compression

One key aspect of numerical modelling studies on layered rock is fracture spacing to layer thickness ratio of layer-bound fracture sets. Opening-mode tensile fractures are common in sedimentary rock, and their spacing is often proportional to the thickness of the fractured layer (Ladeira and Price, 1981; Tang et al., 2008; Wu and Pollard, 1995). Clearly, it would be advantageous for flow prediction if fracture spacing could be inferred from bed thicknesses deduced from drilling (Olson, 2004). The growth of fractures in layered sequences has been described in terms of 'Sequential Infilling', where the term 'Fracture Saturation' is given to the strata when no more fractures can infill even with increasing strain (Bai et al., 2000a).

In this section, a classical three-layer sandwich model (shale-limestone-shale) is taken as the problem domain to study the controls on the fracture spacing in the central competent layer (limestone). The focus is on the modelling of tensile fractures in a competent layer (limestone) surrounded by indirect stretching of the incompetent matrix (shale), in which condition tensile fracturing in the competent layer (limestone) occurs by stress transfer from extension of incompetent neighbouring layers (shale).

4.1 Model setup

The model investigated here has identical dimensions to a case investigated by Tang et al. (2008), where the central layer of 0.03 m thickness is sandwiched between two layers of 0.045 m thickness (Figure 7). All three layers have the same length of 0.6 m. Tang et al. (2008) applied direct tension boundary conditions in the x-direction and set the central layer stiffer but with lower strength than the matrix layers so that tensile fractures initiate first in the central layer. This is because the tensile strains are forced to increase evenly in the inner and outer layers, but with tensile stresses building up to critical values first in the central layer due to greater stiffness. In their model, they introduced heterogeneity of mechanical properties by a Weibull distribution. In this paper the material is assumed to be homogeneous and the material stiffness and strength properties are selected as reasonable for a limestone-shale multilayer (e.g. Engelder and Peacock, 2001). Details of the material properties can be found in Table 1.

Table 1: Material properties used in the three-layer sandwich model.

Rock types	Shale	Limestone
Density ρ (kg·m^{-3})	2400	2700
Young's modulus E (GPa)	10	50
Poisson's ratio υ	0.15	0.25
Tensile strength f_t (MPa)	2	10
Shear strength f_s (MPa)	7	35
Fracture energy G_f (J·m^{-2})	30	50

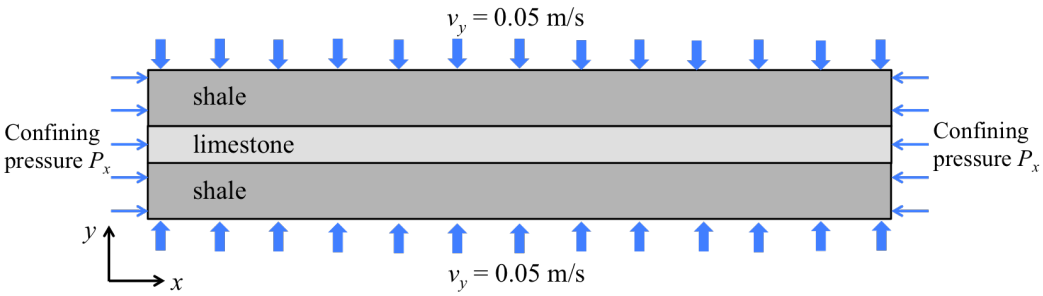

Figure 7: Three-layer model and its boundary conditions.

A layer-normal compressive stress regime is considered. The maximum for the average vertical strain is set at ε_{yy} = 1%. A time-step of 5.0×10^{-8} s ensures stable results with 3-node triangular elements of ~2 mm in the central limestone layer and ~5 mm in the surrounding shale layers. The simulation performed is equivalent to a large composite specimen subjected to a rock mechanics test in a plane strain rig (zero strain in *z*-direction) with constant velocity v_y for the upper and lower boundaries and constant confining pressure P_x for the left and right end boundaries. During the simulation, inelastic as well as elastic stretching in the shale is generated which contributes to tensile stresses being imparted to the central limestone layer. Four values of confining pressures (P_x = 0, 1, 5 and 10 MPa) are modelled to illustrate fracture development in the three-layer model.

The properties of the layer interfaces are significant. On the one hand, welded interfaces, i.e. no slipping or opening is permitted, would result in the multi-layered system behaving as intact rock with some alternating competent and incompetent material properties; however, slipping between beds is an important process given the geological evidence of bedding plane interface shear and pull-apart structures (Price and Cosgrove, 1990). On the other hand, frictionless contacts would preclude shear stress transfer between layers. An alternative is to treat layer interfaces as pre-existing closed cracks with no cohesion, and permit slip to occur according to a frictional contact law. Here a Coulomb friction law (Section 3.2) is adopted and a friction coefficient μ = 0.5 is used for sliding between fracture walls within either rock type as well as for the horizontal interfaces between them.

4.2 Numerical results

The values of average vertical strain ε_{yy}, expressed as percentages identify different stages in each simulation of fracture development as shown in Figure 8 – Figure 11. The first model with no confinement (P_x = 0 MPa, Figure 8) has a very rapid period of formation of multiple tensile fractures and delamination, however damage to the end of the shale layers inhibit tensile fractures from forming near to the ends. The lack of confinement enables the failed model to stretch out smoothly with zero resistance. It should be noted that because the triangular mesh is asymmetric, the fracture patterns are not symmetric as expected from an ideal homogenous domain. Moreover, there is no pre-existing impurities or flaws in the model before fracture initiation, so the

formation of the first fracture is greatly due to numerical perturbation, but it does not affect the sequence of fracture formation afterwards.

The results of confining pressure P_x = 1 MPa are shown with more details in Figure 9. It can be seen that fragments wedging out as end-effects are only slightly suppressed, which is realistic for flexural flow settings of folded multilayers. Figure 9 shows the yielding in the shale is physically expressed as conjugate shear fractures at appropriate bulk σ_{yy} values given by the material properties (see bulk stress-strain curves in Figure 12). The first tensile fracture is initiated by a stress concentration caused by shear displacements in the shale perturbing the lower boundary of the limestone layer at about ε_{yy} = 0.127%, but no fractures have developed in the middle region of the model. Fracture infill is not by idealised model sequential infill as the second and third fractures grow simultaneously. Fracture 4 grows in the centre of the longest intact segment. Fracture 5 initiates (like fracture 1) then 6 grows between 3 and 4, 7 between 4 and 5, 8 between 2 and 5, 9 between 4 and 6, which is in approximate order of longest segment. The peak average vertical stress of ~17.5 MPa at ε_{yy} ~0.120% drops rapidly afterwards (Figure 12), and by ε_{yy} = 0.177%, the 10th and last fracture in the longest unbroken segment of limestone has developed. This phase of very rapid sequential fracture development is accompanied by the main rapid drop in bulk vertical stress (Figure 12). From this point, strain in the limestone is increased by opening of fractures and interface slipping while in the shale, there is steady shear displacement on conjugate shear surfaces and a very slight increase in fracture density. During the long post-fracture saturation phase of fracture opening, the longer limestone segments suffer bending stresses; these are not sufficient to initiate further tensile fractures, but could explain the stress fluctuations between 0 and 5 MPa (Figure 12).

The third model is highly confined (P_x = 5 MPa, Figure 10). The initial pressure pulse sets up a transient stress wave as seen in the pre-peak loading curve and various vibration modes with stress amplitudes below those for yielding (Figure 12). Onset of tensile fracturing in the limestone layer near the left end is at a higher peak average stress (~20 MPa) and ε_{yy} = 0.145%; thereafter orderly sequential infilling develops as each longest segment fractures first. After fracture 11 and 14, longer periods of straining in the shale precede the next fracture. Resistance to continued layer normal shortening falls to a post peak value of ~11 MPa by ε_{yy} = 0.350% with stress fluctuations of higher amplitude possibly associated with more significant stick-slip

frictional events. Fractures continue to infill in the limestone after this point. Detailed observation shows that fractures in the limestone often propagate away from a perturbation at the shale boundary for over several mesh elements and with a significant shear component on the advancing crack before a local tensile stress ahead of the crack tip redirects the crack orientation towards the *y*-direction. This shear initiation at these higher mean stresses appears to provide a new mechanism to continue splitting the limestone at the higher strain levels.

The last model (P_x = 10 MPa, Figure 11) can be understood with reference to Figure 12 and Figure 13 as a more extremely confined case than the third case (P_x = 5 MPa), with frictional behaviour even more dominant, and the shale exhibiting a diffuse shear fracture refined down to element size level towards the later stages. Figure 11 shows that by ε_{yy} = 0.200% only three fractures have formed in the limestone during the main stress drop. Frictional resistance to shearing in the shale maintains the residual bulk stress at ~17 MPa with additional fracturing in the limestone appearing to reaching saturation between ε_{yy} of 0.800% and 1.000% (Figure 13) with an average spacing to layer thickness ratio S/t_f of ~0.8, where S is the average distance between fractures in the central limestone layer, and t_f is the thickness of this layer, which equals 0.03 m.

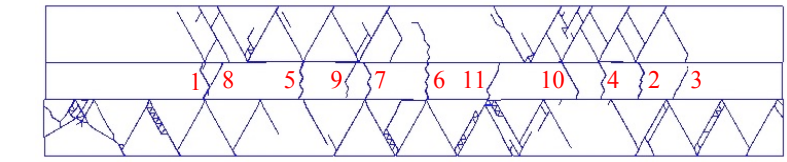

a. ε_{yy} = 0.198%.

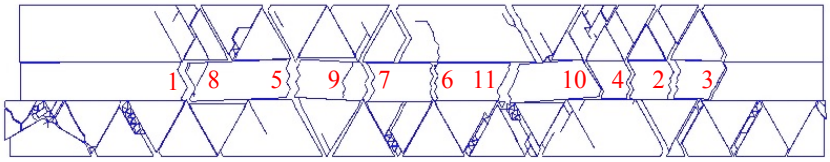

b. ε_{yy} = 1.000%.

Figure 8: Numerical simulation stages of fracture patterns forming with confining pressure 0 MPa. Note that shear fractures develop in the shale and the limestone develops tensile fractures which infill in a sequence (see numerals in red colour).

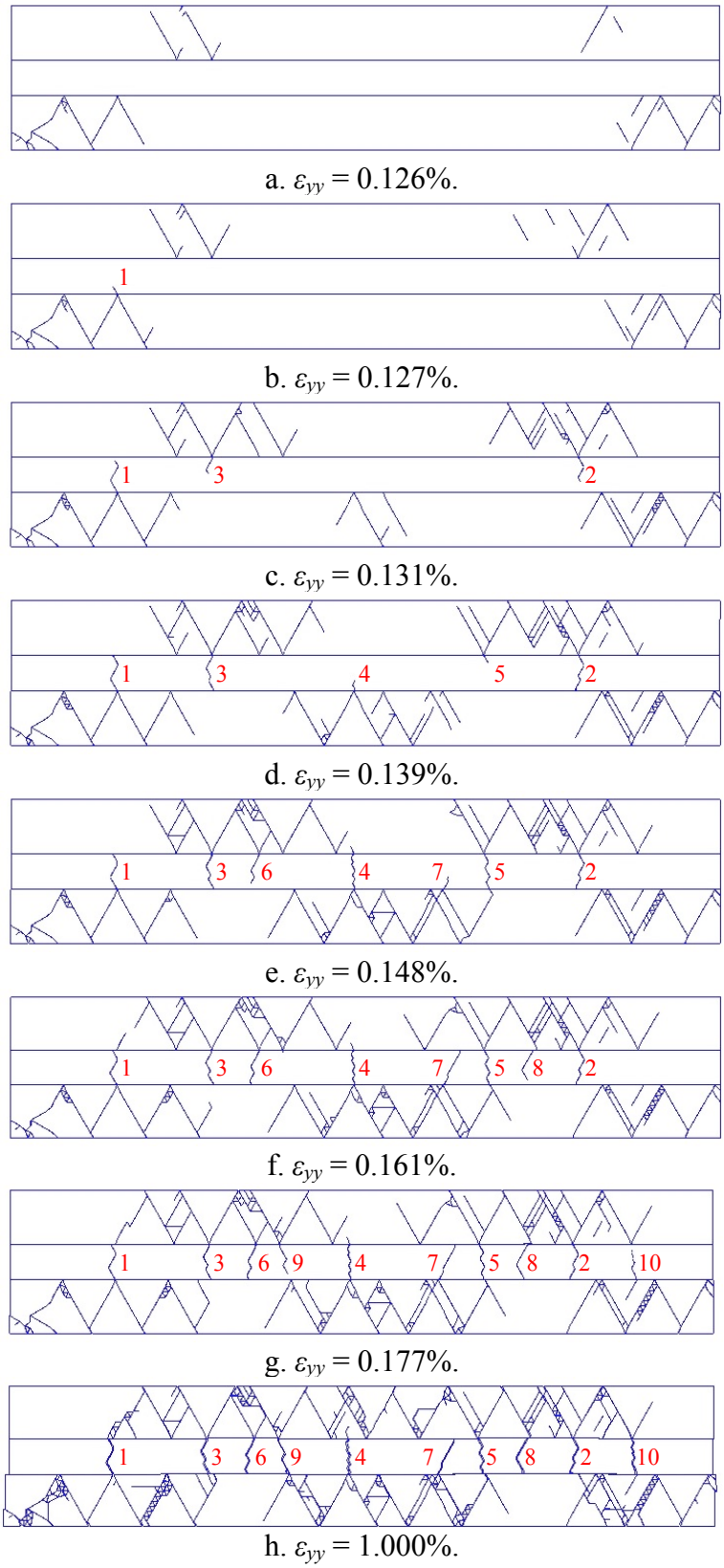

Figure 9: Fracture development in the three-layer model with confining pressure 1 MPa. The numerals in red colour identify the sequence of fracture formation.

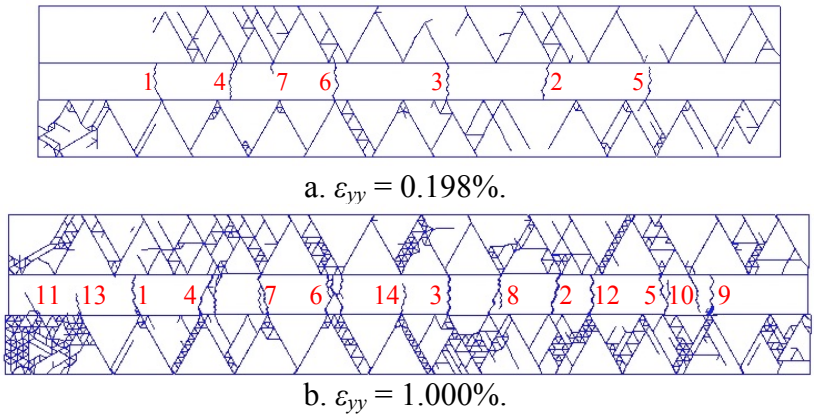

a. $\varepsilon_{yy} = 0.198\%$.

b. $\varepsilon_{yy} = 1.000\%$.

Figure 10: Fracture development in the three-layer model with confining pressure 5 MPa.

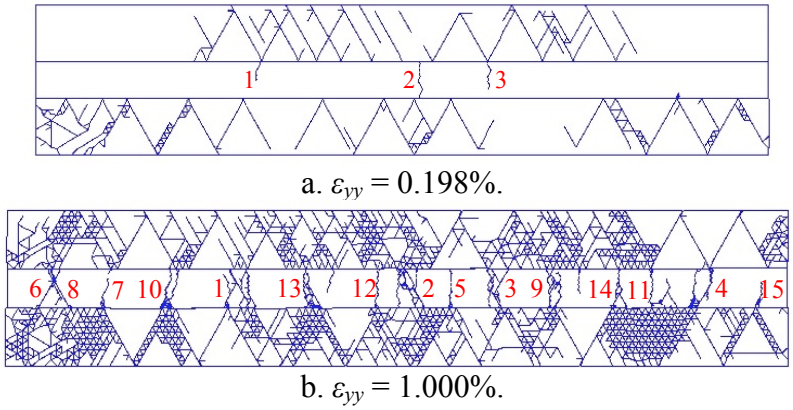

a. $\varepsilon_{yy} = 0.198\%$.

b. $\varepsilon_{yy} = 1.000\%$.

Figure 11: Fracture development in the three-layer model with confining pressure 10 MPa.

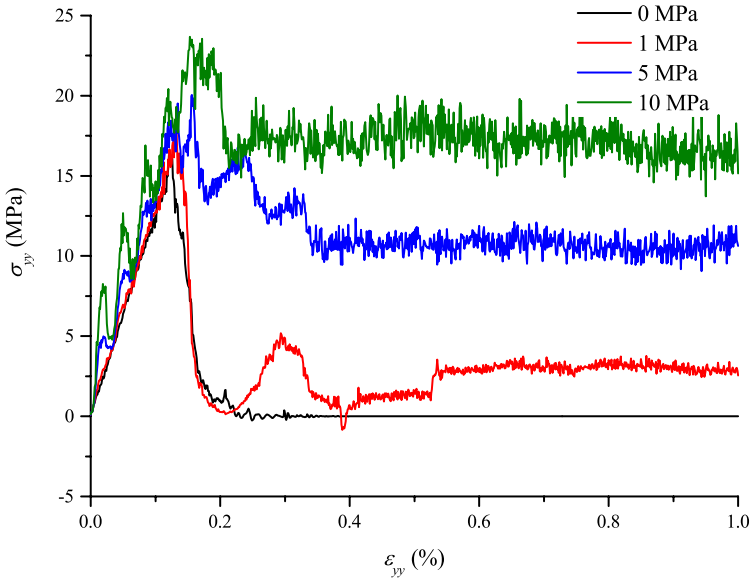

Figure 12: Bulk stress versus vertical strain (normal to layering) is shown for different confining pressures acting parallel to the layers.

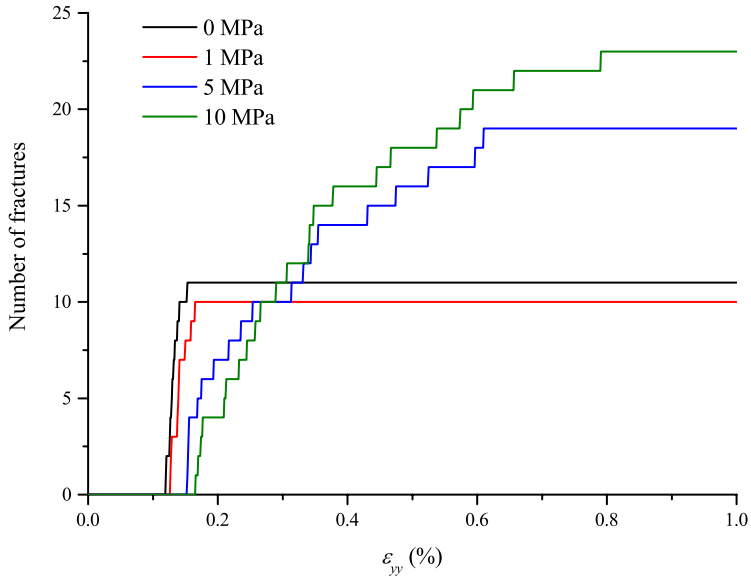

Figure 13: Accumulation of numerically modelled fractures in the central (limestone) layer. Note that saturation happens after a certain number of fractures.

The numerical results show that average fracture spacing to layer thickness ratio S/t_f at saturation is 1.8 (P_x = 0 MPa) and 1.7 (P_x = 1 MPa) for the lower confining pressure cases similar to that for the homogeneous case obtained by Tang et al. (2008). At higher confinement, however, the mean stress is higher, and normal stresses across the frictional layer interface inhibit sliding so that for P_x = 5 MPa, S/t_f = 1.0 and at P_x = 10 MPa, S/t_f = 0.8; these fractures are more clustered into swarms or zones.

Layered rocks undergoing increasing layer-normal compression during slow burial in a geological basin setting may develop a steady inelastic deformation in the shale layers as they yield and stretch pervasively or they may deform with more localised shearing deformation styles. One limitation of the numerical model used in this paper is that failure of material can only be characterised by developing discrete fractures, while in this case of shale layers, material deformation may look more realistic if they are characterised by forming shear bands (plastic strain localisation). However, here the focus is to investigate the tensile fracture spacing in the central limestone layer, by using the three-layer setup to generate a realistic stress regime, and the inelastic deformation in the shale layers has been simulated by explicitly forming conjugate shear fractures. Although the shear fracture patterns are not exactly the same as field observations, from Figure 12 it can be seen that the bulk stress – strain relations are correct responses to the boundary conditions.

A possible mechanism favouring $S/t_f < 0.8$ is suggested by those models at higher confining pressures. Under the higher mean stresses, shear fractures in the shale normally arrested by the limestone, often promote stress concentrations and shear fractures, which eventually propagate into the competent limestone across the boundaries. These shear fractures in the limestone which are initiated near the shale-limestone boundaries amplify the stresses at the advancing fracture tips. The fractures transform back from shear mode into tensile mode as they straighten towards the direction of maximum compressive stress and propagate through the otherwise compressed material. The high reported incidence of $S/t_f < 0.8$ in geological sedimentary sequences (Bai and Pollard, 2000a, 2000b) could also be explained by internal fluid pressures in the Earth's crust; high internal fluid pressure could cause effective stress to change its mode from compression to tension, which will generate tensile fractures once it reaches the rock material's tensile strength.

5 Through-going fracture formation under layer parallel tension and bending

This section focuses on another key aspect of numerical studies on layered rock – the formation of through-going fractures across layer interfaces, which plays an important role in vertical fluid migration across and within sedimentary rock layers. The model simulated in this section corresponds to a seven-layer horizontal limestone composite sampled from the vertical section of a large wavelength fold (Price and Cosgrove, 1990). The scale of the sampled composite is considerably smaller than the scale of the major fold, so layer curvature can be neglected.

5.1 Model setup

The model investigated here is a seven-layer all-limestone sequence (Figure 14), in which the layers are numbered in an ascending order from the upper layer to the lower layer. The light and dark grey colours represent two types of limestone with an approximate 20% difference in material properties (Table 2, Atkinson, 1987; Lama and Vutukuri, 1978; Zoback, 2010). The material within each horizontal layer is assumed as isotropic and homogeneous material. The length of the model is 0.6 m and the thickness of the whole model is 0.2 m, which consists of layers 1, 3, 5 and 7 of 0.02 m thickness and layers 2, 4 and 6 of 0.03 m, 0.04 m and 0.05 m thickness,

respectively. All of the seven layers are meshed using unstructured 3-node triangular elements with an average size of 2 mm. A time-step of 1.0×10^{-8} s is used in the numerical modelling. A Coulomb friction law is applied to govern both sliding between opposite sides of a fracture and sliding on an interface between layers; the friction coefficient μ is set to be 0.6.

Table 2: Material properties used in the seven-layer model.

Layer numbers	1, 3, 5 and 7	2, 4 and 6
Density ρ (kg·m^{-3})	2500	2700
Young's modulus E (GPa)	50	60
Poisson's ratio υ	0.25	0.35
Tensile strength f_t (MPa)	4.2	5.0
Cohesion c (MPa)	10	12
Internal friction angle ϕ (°)	25	30
Fracture energy G_f (J·m^{-2})	50	60

5.2 Numerical results of direct tension

In the first example shown in Figure 14, a loading condition of direct tension parallel to the material layers is applied to the model. The left end boundary is fixed in the x-direction, and the lower boundary is fixed in the y-direction. A velocity-controlled constraint condition in the x-direction v_x is applied to the right-hand boundary, and different pressures in the y-direction P_y ranging from 0 MPa to 10 MPa are applied to the upper boundary. Both the velocity and pressure conditions are applied as a linear ramp-up from zero to the designed boundary constraint values over the first 0.002 s in the numerical modelling to reduce the impact effect when loading suddenly starts.

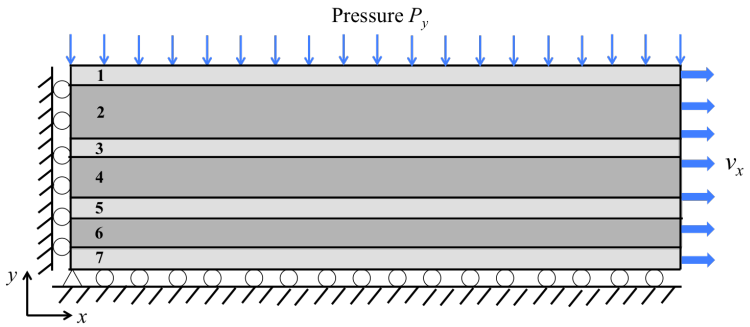

Figure 14: Seven-layer model undergoing direct tension parallel to layers.

The values of mean horizontal strain ε_{xx} are used to identify different stages in fracture development as shown in Figure 15 – Figure 18. The tensile strains in the *x*-direction are forced to increase evenly in all seven layers by the uniform velocity loading conditions at the right end boundary. Although tensile stresses developed in the thin, weaker layers (layer 1, 3, 5 and 7) are smaller than the thicker layers, the tensile strength of layer 1, 3, 5 and 7 is also smaller. For the case of zero pressure in the *y*-direction (Figure 15), the tensile fractures first initiate in the thinner layers. Then more tensile fractures subsequently grow in the thick layers, however none are connected across interfaces with fractures in neighbouring layers. When no new fractures are generated with increasing strain, most layers have only one fracture. This is because stress is no longer transferred from the right end boundary after the model has been totally pulled apart. Fractures can be seen to link from the top to the bottom and these will simply open up with further applied strain. According to the numerical method used in the simulations, fractures can only propagate along element edges, so this mesh dependency in an unstructured mesh results in asymmetry of the fracture patterns.

Figure 16 – Figure 18 show the results of models with non-zero pressures in the *y*-direction, which are introduced to model the effect of layer-normal compression during slow burial in a geological basin setting. At an early stage, the most significant difference compared with the $P_y = 0$ MPa model is that tensile fractures initiate almost simultaneously both in thick and thin layers in the upper part of the model. This preferential position of initial fractures is caused by the fact that the pressures in the vertical direction are applied at the upper boundary, which results in an additional layer horizontal extension being sensed first at the top slightly before the reaction force is taken up at the bottom. For greater values of P_y, fracture generation becomes more localised with fracture connection across layer interfaces occurring. For $P_y = 1$ MPa, fractures propagate across layer interfaces in two layers (layer 4 and 5, layer 6 and 7, respectively); for $P_y = 5$ MPa, fractures propagate across layer interfaces in three layers (layer 3, 4 and 5); for $P_y = 10$ MPa, fractures propagate across layer interfaces in five layers (layer 3 – 7).

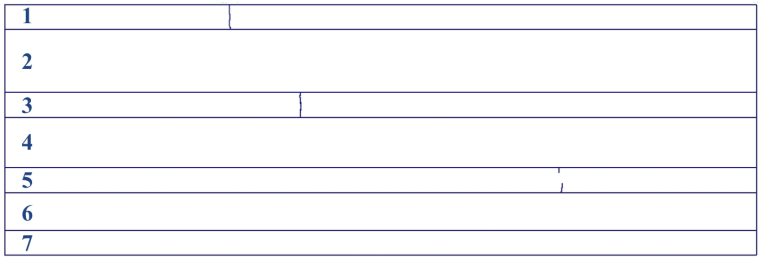

a. $\varepsilon_{xx} = 0.013\%$.

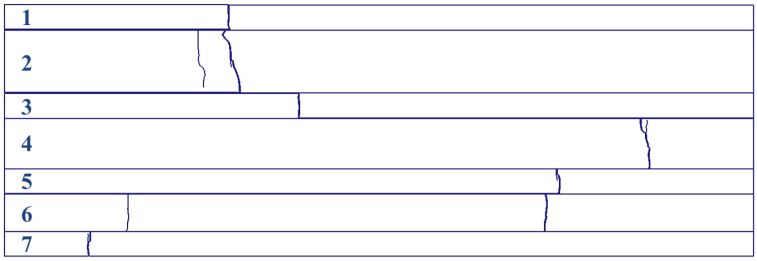

b. $\varepsilon_{xx} = 0.107\%$.

Figure 15: Numerical results of fracture patterns forming in the seven-layer model subject to direct tension parallel to the layering with vertical pressure 0 MPa.

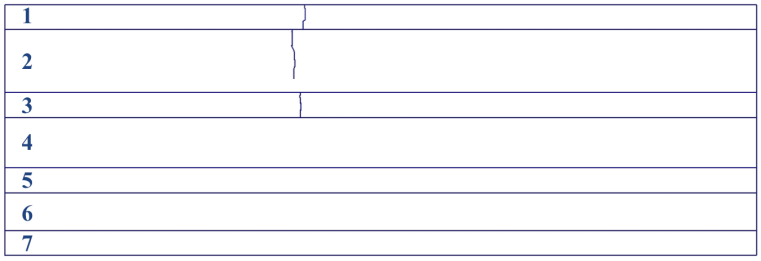

a. $\varepsilon_{xx} = 0.015\%$.

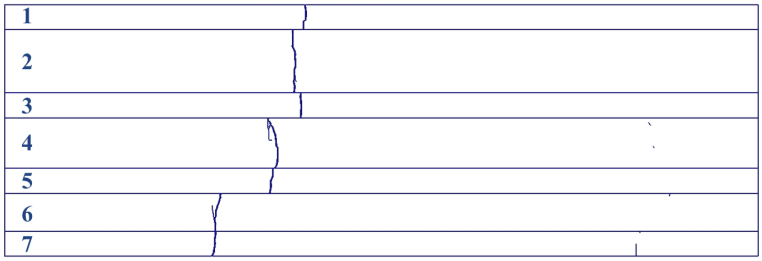

b. $\varepsilon_{xx} = 0.107\%$.

Figure 16: Fracture formation in the seven-layer model subject to direct tension with vertical pressure 1 MPa.

a. $\varepsilon_{xx} = 0.020\%$.

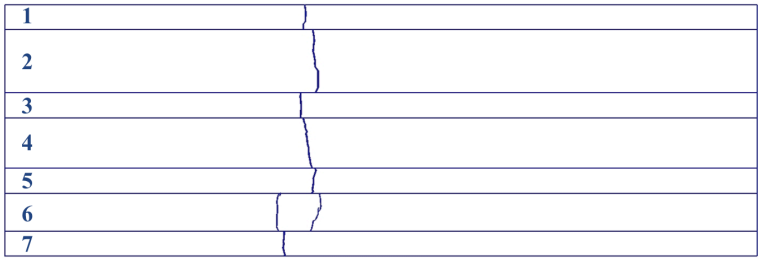

b. $\varepsilon_{xx} = 0.107\%$.

Figure 17: Fracture formation in the seven-layer model subject to direct tension with vertical pressure 5 MPa.

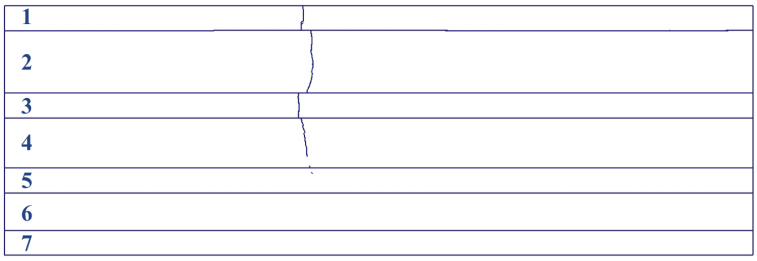

a. $\varepsilon_{xx} = 0.026\%$.

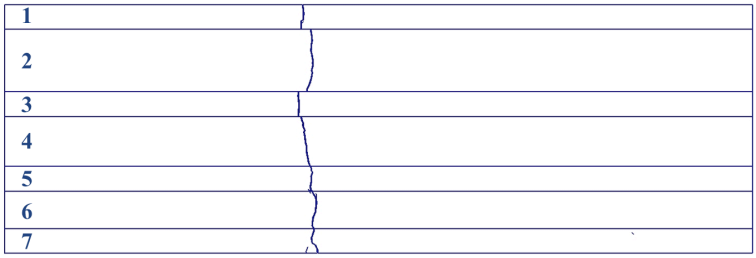

b. $\varepsilon_{xx} = 0.107\%$.

Figure 18: Fracture formation in the seven-layer model subject to direct tension with vertical pressure 10 MPa.

Fracture aperture plays an important part in permeability analysis of geological systems and also provides a perspective to explicitly investigate the delamination of layer interfaces if they are viewed as pre-existing closed cracks with no cohesion. In this simulation, fracture apertures can be extracted in the post-processing (Lei et al., 2014). The normal apertures of models subject to direct tension with pressure $P_y = 0$ MPa and 10 MPa are shown in Figure 19, which correspond to the fracture patterns in

Figure 15 and Figure 18. When P_y = 0 MPa, all the major tensile fractures are fully developed and largely opened to ~0.7 mm. The second tensile fractures in layer 2 and layer 6 are just opened to ~0.1 mm, which is due to the cessation of stress transfer from the right end boundary. The wide-open fractures and fully delaminated interfaces together provide potential paths for relatively rapid fluid flow. A section of the model (Figure 19a) is extracted to investigate the relation between the timing of fracture initiation and layer interface delamination. The bulk horizontal stresses of layer 2 and 3, as well as normal aperture at the interface between layer 2 and 3 in this section, is plotted versus bulk horizontal strain in Figure 20. The plot suggests that it is the critical difference in horizontal stresses in the two layers that initiates delamination followed by aperture opening. The initiation of the first fracture in each layer is accompanied by a rapid drop in bulk horizontal stress. The increase in normal aperture indicates the delamination at the layer interface, which happens just after the initiation of fractures in both layers. This indicates interface delamination occurs after the fracture initiation in the neighbouring layers on both sides of the interface. It should be noted that the tensile strengths in Figure 20 are slightly higher than the input values assigned as material properties. This is because the loading is not strictly static so the materials are somewhat stronger, but the fracture behaviour is essentially similar for a range of engineering type loading rates. It is also worth noting that stress fluctuations at post-peak stages in Figure 20 indicate stick-slip frictional events between layer 2 and 3.

The model with pressure P_y = 10 MPa (Figure 19b) has no delamination at interfaces because of the high pressure in the *y*-direction, which clearly proves that vertical stress has a significant influence on the delamination at horizontal layer interfaces. Moreover, another phenomenon significantly influenced by vertical pressures is the formation of through-going fractures, which are important for fluid flow analysis in multi-layered systems. Low vertical stress enables the interface between fractured and non-fractured layers to delaminate, which can impede tensile fracture propagation across an interface (Figure 21, Casabianca and Cosgrove, 2012).

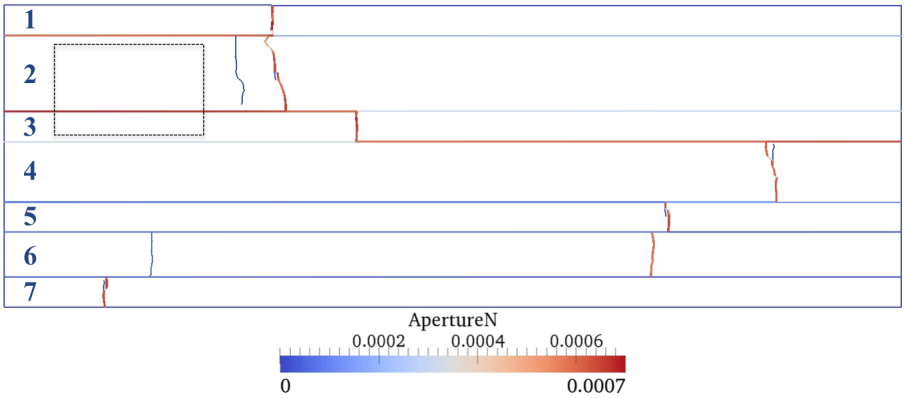

a. P_y = 0 MPa, ε_{xx} = 0.107%. The dashed frame extracts a section for stress and aperture analysis in Figure 20.

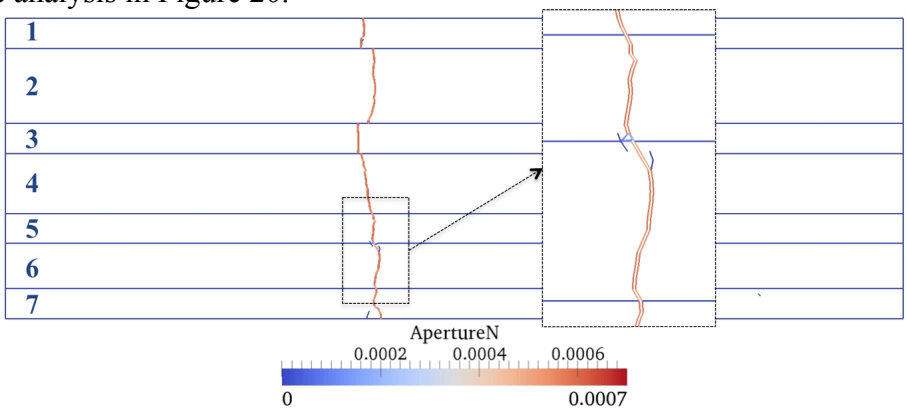

b. P_y = 10 MPa, ε_{xx} = 0.107%. Note that a through-going fracture across the interfaces of layer 4-7 is shown in detail.

Figure 19: Normal apertures (unit: m) of the seven-layer model subject to direct tension parallel to the layering.

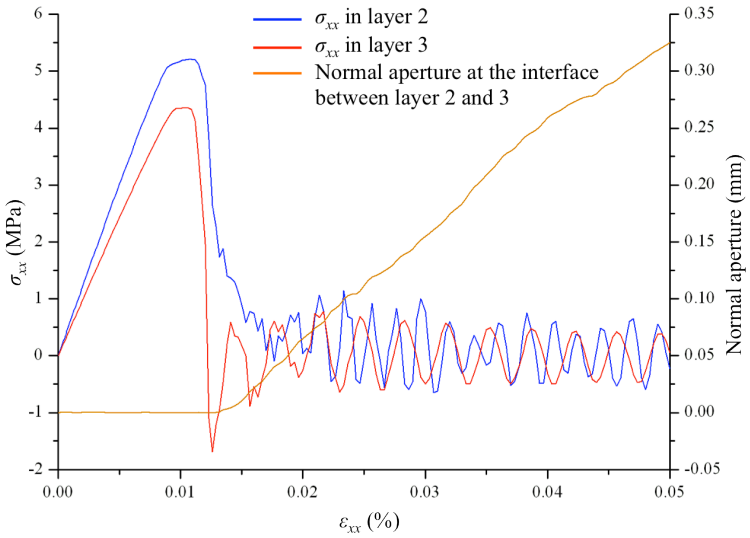

Figure 20: Horizontal stress and normal aperture of the section extracted from Figure 19a.

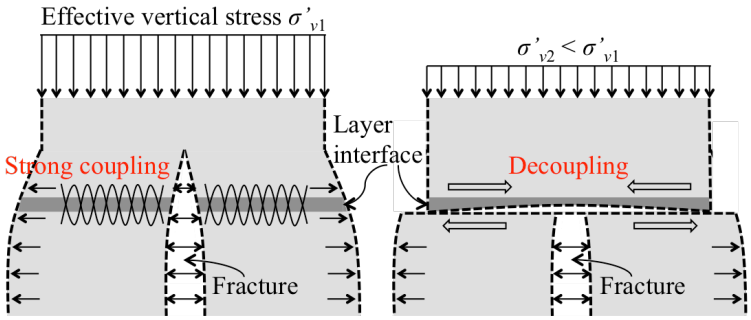

Figure 21: Schematic illustration of the influence of effective vertical stress on the formation of through-going fractures.

5.3 Numerical results of bending

In the second example, two bending conditions are modelled. In both cases, the seven-layer model is pushed up by a point velocity in the y-direction v_y at the middle point of the lower boundary. It can be seen from Figure 22 that the only difference between these two models lies in the boundary constraint conditions at the left and right ends. In Figure 22a, the two ends of the model are clamped, which means both the translation and rotation are constrained, while in Figure 22b, the constraints are similar to a three-point bending test with differential displacements possible at the layer ends.

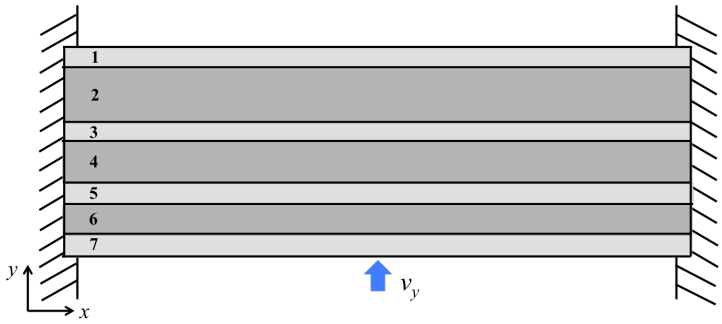

a. Two ends are clamped; in this case, the layer ends are completely fixed.

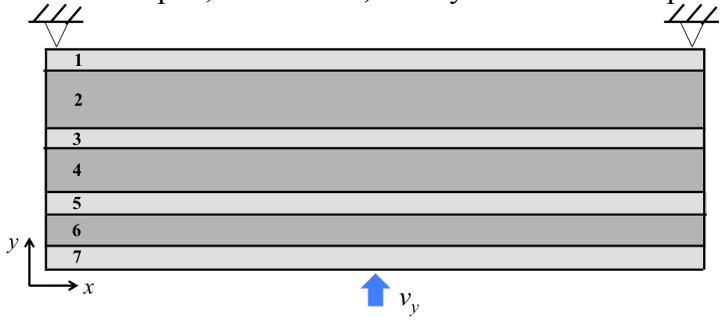

b. Two ends are not clamped; in this case, the layer ends can rotate.

Figure 22: Bending conditions of the seven-layer model.

The contour plot of the horizontal stress component σ_{xx} of the clamped model (Figure 23a) shows that before the first fracture initiates, the seven-layer model has come to a state that there exists a neutral surface in every layer, which separates the tensile and compressive stress fields. However, in the middle region of every layer the upper part is in tension and the lower part is in compression, but at the left and right ends it is the opposite distribution because of the clamped boundary constraints. The tangential longitudinal strain model is reasonably well exhibited throughout all layers. When fractures start to initiate and until fractures have saturated (Figure 23b), mainly tensile fractures develop in the tensile stress fields and shear fractures develop in the compressive stress fields. Due to the mesh dependency of the fracture orientation, a few very short shear fractures of one or two element edge length are distributed along the tensile fracture paths; other than that, the length of both tensile and shear fractures are proportional to the layer thickness.

The un-clamped model exhibits typical behaviour of a three-point bending beam for every layer. The horizontal stress contour prior to fracture initiation (Figure 24a) shows a different pre-failure state compared with the clamped model. Although the middle region of every layer has a similar stress distribution to the clamped model, the left and right ends are almost free of horizontal stress, a consequence of the constraint-free boundary conditions. These different horizontal stress distributions govern the difference in fracture patterns (Figure 24b). The un-clamped model has only one through-going tensile fracture in the middle, though separated by a few very short shear fractures due to mesh dependency as noted in Figure 23b.

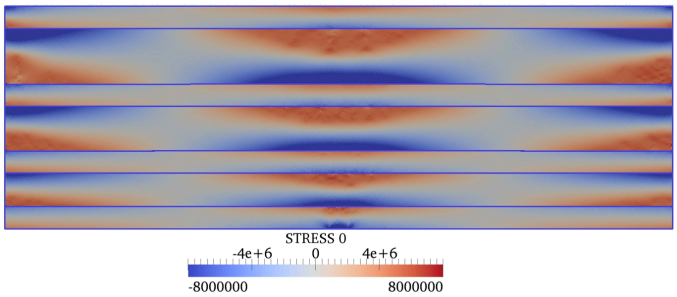

a. Clamped model before fracture initiation.

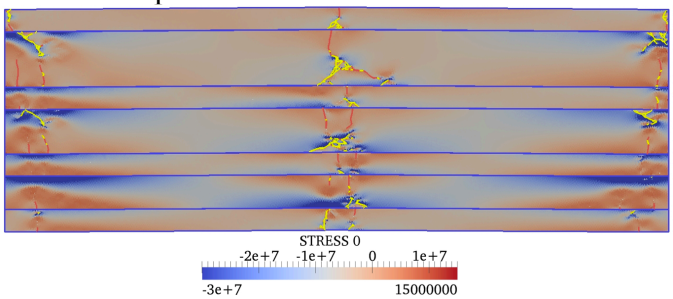

b. Clamped model at fracture saturation.

Figure 23: Horizontal stress contours σ_{xx} (unit: Pa) and fracture patterns of the seven-layer model subject to bending. For the fracture patterns, the red colour represents tensile fractures; the yellow colour represents shear fractures; and the blue colour represents layer interfaces and model boundaries.

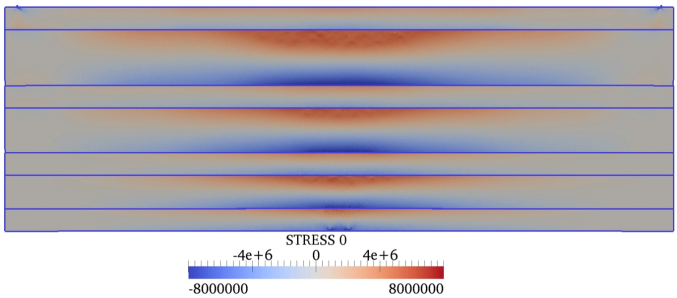

a. Un-clamped model before fracture initiation.

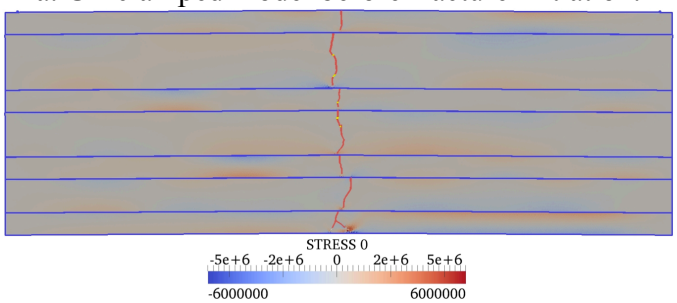

b. Un-clamped model at fracture saturation.

Figure 24: Horizontal stress contours and fracture patterns of the seven-layer un-clamped model subject to bending.

To summarise the differences, in the freely un-clamped model (Figure 24b), although a neutral surface associated with Tangential Longitudinal Strain (TLS) is

seen to develop in all layers prior to fracture, once tensile fractures initiate in the tensile zone (almost simultaneously in all layers), the freely rotating limb boundary conditions permit interlayer slip causing the inner-arc compression zones to relax, and the neutral surface migrates as the tensile cracks propagate with further bending. Compression is unable to build significantly on the inner-arcs once outer-arc fracture has propagated and shifted the neutral surface. Returning to the clamped model (Figure 23b), it is clear that the models are quite similar up until fracture initiation, but in this case the TLS patterns are developed and retained well after the first fractures start to form. This is because there is no slip allowed, and the inner-arc compressive stresses cannot be relieved through interlayer slip as further amplification occurs.

Although quite different to conventional layer compression models associated with the production of buckle folds, the models studied here were subject to different forms of bending. Noting that the through-going fractures in the hinge region are in one case developed and in another are not, the boundary conditions promoting the through-going fractures are suggested to be more likely to exist in forced folding of layered rocks where interlayer slip is available. This can then act as a mechanism for accommodating strain, relieving compression zones, and resulting in the tensile cracks propagating fully across the layers.

With respect to forced folding in geological sequences with units of very low competence contrasts such as in limestone sequences, the modelling results provoke some speculation. It is suggested that significant through-going fractures in the hinge are more likely where slip on interfaces between main structural units is uninhibited. It might be argued that this is more likely in a sequence where structural units are thinner with respect to the span of the folded region. In contrast, and by the same reasoning, it could be suggested that thicker units giving rise to stubbier looking fold structures that suppress rotation and interface sliding, in addition to outer-arc fracture, might be more inclined to express inner-arc compressive deformation features, whether by shear failure or, perhaps more likely, by pressure solution seam development.

6 Conclusions

Facture spacing and through-going fracture formation in layered rocks were simulated using a fracture model that combines the finite element formulation and the discrete element formulation. First, the controls on fracture spacing to layer thickness ratio in a three-layer shale-limestone-shale sequence undergoing layer normal compression was examined with foci on frictional sliding on shear fractures within incompetent rock (shale) and tensile fracturing in competent rock (limestone). Fracture spacing to layer thickness ratios at fracture saturation from 1.8 to 0.8 were obtained for different confining pressures considered in the modelling. These were compatible with both high and low ratios observed from geological sequences. This work also suggested layer interface properties and behaviour cannot be considered negligible in layered rocks because the delamination at the interface and slipping between layers contributed to fracture pattern development.

Second, the formation of through-going fractures was modelled in a seven-layer limestone model with low competence contrast under direct tension and bending conditions. The results showed that in layered rocks undergoing layer parallel tension, delamination at layer interfaces normally occurred after fracture initiation had taken place on each side of the interface. Higher effective stresses that are perpendicular to the layering enabled fractures to propagate across layer interfaces to form through-going fractures. It also suggested that through-going fractures were more likely to exist in forced folding of layered rocks where interlayer slip is available.

It has been demonstrated by the numerical results that the FEMDEM method is capable of generating fracture patterns according to geomechanical principles of rock failure, and also realistically modelling the frictional behaviour at interfaces in layered rocks. This fracture model, together with various post-processing programs, e.g. fracture visualisation, aperture extraction, etc., provides an ideal tool to investigate in detail the formation of fracture patterns as well as slipping and delamination in layered rocks. It should be noted that the constitutive model used for the interface elements is only applicable to loading conditions without unloading paths; in the future, a more complicated model including possibility of unloading (e.g. Pouya and Bemani Yazdi, 2015) will be implemented into the numerical code. It is also worth mentioning that a number of three-dimensional fracture models have been developed in recent years (Guo et al., 2015; Rabczuk et al., 2010). In the future,

similar numerical studies can be extended into three-dimensional modelling, which could give an insight into the understanding of more realistic and complicated scenarios.

Acknowledgements

We are grateful for the support from Janet Watson scholarship provided by the Department of Earth Science and Engineering, Imperial College London for the PhD project of the first author. The research has greatly benefited from other research projects hosted by AMCG (Applied Modelling and Computation Group) at Imperial College London that were running in parallel with this PhD study, notably the itf-ISF oil company consortium on fractured reservoirs.

References

Atkinson, B. K., 1987. Fracture mechanics of rock, Academic Press.

Bai, T., Pollard, D. D., 2000a. Fracture spacing in layered rocks: a new explanation based on the stress transition. Journal of Structural Geology 22, 43-57.

Bai, T., Pollard, D. D., 2000b. Closely spaced fractures in layered rocks: initiation mechanism and propagation kinematics. Journal of Structural Geology 22, 1409-1425.

Bai, T., Pollard, D. D., Gao, H., 2000a. Explanation for fracture spacing in layered materials. Nature 403, 753-756.

Bai, T., Pollard, D. D., Gross, M. R., 2000b. Mechanical prediction of fracture aperture in layered rocks. Journal of Geophysical Research 105(B1), 707-721.

Becker, A., Gross, M. R., 1996. Mechanism for joint saturation in mechanically layered rocks: an example from southern Israel. Tectonophysics 257, 223-237.

Belytschko, T., Black, T., 1999. Elastic crack growth in finite elements with minimal remeshing. International Journal for Numerical Methods in Engineering 45, 601-620.

Bittencourt, T. N., Wawrzynek, P. A., Ingraffea, A. R., Sousa, J. L., 1996. Quasi-automatic simulation of crack propagation for 2D LEFM problems. Engineering Fracture Mechanics 55(2), 321-334.

Bocca, P., Carpinteri, A., Valente, S., 1991. Mixed mode fracture of concrete. International Journal of Solids and Structures 27(9), 1139-1153.

Bonet, J., Wood, R. D., 1997. Nonlinear Continuum Mechanics for Finite Element Analysis, first ed. Cambridge University Press, Cambridge.

Bordas, S., Rabczuk, T., Goangseup, Z., 2008. Three-dimensional crack initiation, propagation, branching and junction in non-linear materials by an extended meshfree method without asymptotic enrichment. Engineering Fracture Mechanics 75, 943-960.

Casabianca, D., Cosgrove, J., 2012. A new method for top seals predictions in high-pressure hydrocarbon plays. Petroleum Geoscience 18, 43-57.

Coggan, J. S., Stead, D., Gao, F., 2014. Numerical modelling of brittle fracture in geological materials, in: Proceedings of the 22nd UK Conference of the Association for Computational Mechanics in Engineering. Exeter, UK, pp. 133-136.

Cundall, P. A., Strack, O. D. L., 1979. The development of constitutive laws for soils using distinct element method, in: Proceedings of the 3rd Numerical Methods in Geomechanics. Aachen, Germany.

Das, R., Cleary, P. W., 2010. Effect of rock shapes on brittle fracture using smoothed particle hydrodynamics. Theoretical and Applied Fracture Mechanics 53, 47-60.

de Borst, R., 2003. Numerical aspects of cohesive-zone models. Engineering Fracture Mechanics 70, 1743-1757.

Doolin, D. M., Mauldon, M., 2001. Fracture permeability normal to bedding in layered rock masses. International Journal of Rock Mechanics & Mining Sciences 38, 199-210.

Engelder, T., Peacock, D. C., 2001. Joint development normal to regional compression during flexural-flow folding: the Lilstock Buttress Anticline, Somerset, England. Journal of Structural Geology 23, 259-277.

Farsi, A., Xiang, J., Latham, J.-P., Pullen, A. D., Carlsson, M., Stitt, E. H., Marigo, M., 2015. An application of the finite-discrete element method in the simulation of ceramic breakage: methodology for a validation study for Alumina specimens, in: Oñate, E. et al. (Eds.), PARTICLES 2015, Proceedings of the IV International Conference on Particle-based Methods – Fundamentals and Applications. International Center for Numerical Methods in Engineering (CIMNE), Barcelona, Spain, pp. 921-932.

Finn, M. D., Gross, M. R., Eyal, Y., Draper, G., 2003. Kinematics of throughgoing fractures in jointed rocks. Tectonophysics 376, 151-166.

Fleming, M., Chu, Y. A., Moran, B., Belytschko, T., 1997. Enriched element-free Galerkin methods for crack tip fields. International Journal for Numerical Methods in Engineering 40, 1483-1504.

Fossen, H., 2010. Structural Geology, first ed. Cambridge University Press, New York.

Francfort, G. A., Marigo, J.-J., 1998, Revisiting brittle fracture as an energy minimization problem. Journal of the Mechanics and Physics of Solids 46(8), 1319-1342.

Gray, J. P., Monaghan, J. J., Swift, R. P., 2001. SPH elastic dynamics. Computer Methods in Applied Mechanics and Engineering 190, 6641-6662.

Griffith, A. A., 1921. The phenomena of rupture and flow in solids. Philosophical

Transactions of the Royal Society of London. Series A, Containing Papers of a Mathematical or Physical Character 221, 163-198.

Gross, M. R., Eyal, Y., 2007. Throughgoing fractures in layered carbonate rocks. GSA bulletin 119(11/12), 1387-1404.

Guo L., 2014. Development of a three-dimensional fracture model for the combined finite-discrete element method, PhD thesis, Imperial College London.

Guo, L., Latham, J.-P., Xiang, J., 2015. Numerical simulation of breakages of concrete armour units using a three-dimensional fracture model in the context of the combined finite-discrete element method. Computers & Structures 146, 117-142.

Guo, L., Xiang, J., Latham, J.-P., Izzuddin, B., 2016. A numerical investigation of mesh sensitivity for a new three-dimensional fracture model within the combined finite-discrete element method. Engineering Fracture Mechanics 151, 70-91.

Helgeson, D. E., Aydin, A., 1991. Characteristics of joint propagation across layer interfaces in sedimentary rocks. Journal of Structural Geology 13(8), 897-911.

Hillerborg, A., Modéer, M., Petersson, P.-E., 1976. Analysis of crack formation and crack growth in concrete by means of fracture mechanics and finite elements. Cement and Concrete Research 6, 773-782.

Ingraffea, A. R., Manu, C., 1980. Stress-intensity factor computation in three dimensions with quarter-point elements. International Journal for Numerical Methods in Engineering 15, 1427-1445.

Karihaloo, B. L., Xiao, Q. Z., 2003. Modelling of stationary and growing cracks in FE framework without remeshing: a-state-of-the-art review. Computers & Structures 81, 119-129.

Ladeira, F. L., Price, N. J., 1981. Relationship between fracture spacing and bed thickness. Journal of Structural Geology 3, 179-183.

Lama, R. D., Vutukuri, V. S., 1978. Handbook on mechanical properties of rocks: testing techniques and results, Trans Tech Publications.

Lei, Q., Latham, J.-P., Xiang, J., Tsang, C.-F., Lang, P., Guo, L., 2014. Effects of geomechanical changes on the validity of a discrete fracture network representation of a realistic two-dimensional fractured rock. International Journal of Rock Mechanics & Mining Sciences 70, 507-523.

Ma, G. W., Wang, X. J., Ren, F., 2011. Numerical simulation of compressive failure of heterogeneous rock-like materials using SPH method. International Journal of Rock Mechanics & Mining Sciences 48, 353-363.

Melenk, J. M., Babuška, I., 1996. The partition of unity finite element method: basic theory and applications. Computer Methods in Applied Mechanics and Engineering 139, 289-314.

Min, K.-B., Rutqvist, J., Tsang, C.-F., Jing, L., 2004. Stress-dependent permeability of fractured rock masses: a numerical study. International Journal of Rock Mechanics & Mining Sciences 41, 1191-1210.

Morris, J. P., Rubin, M. B., Blair, S. C., Glenn, L. A., Heuze, F. E., 2004. Simulations of underground structures subjected to dynamic loading using the distinct element method. Engineering Computations 21, 384-408.

Munjiza, A., 2004. The combined finite-discrete element method, first ed. Wiley and Sons, New York.

Munjiza, A., Andrews, K. R. F., 1998. NBS contact detection algorithm for bodies of similar size. International Journal for Numerical Methods in Engineering 43, 131-149.

Munjiza, A., Andrews, K. R. F., 2000. Penalty function method for combined finite-discrete element systems comprising large number of separate bodies. International Journal for Numerical Methods in Engineering 49, 1377-1396.

Munjiza, A., Andrews, K. R., White, J. K., 1999. Combined single and smeared crack model in combined finite-discrete element analysis. International Journal for Numerical Methods in Engineering 44, 41-57.

Munjiza, A., John, N. W. M., 2002. Mesh size sensitivity of the combined FEM/DEM fracture and fragmentation algorithms. Engineering Fracture Mechanics 69, 281-295.

Munjiza, A., Owen, D. R. J., Bicanic, N., 1995. A combined finite-discrete element method in transient dynamics of fracturing solids. Engineering Computations, 12(2), 145-174.

Nelson, R. A., 2001. Geological analysis of naturally fractured reservoirs, second ed. Gulf Professional Publishing, Houston.

Olson, J. E., 2004. Predicting fracture swarms – the influence of subcritical crack growth and the crack-tip process zone on joint spacing in rock, in: Cosgrove, J. W., Engelder, T. (Eds.), The Initiation, Propagation, and Arrest of Joints and Other Fractures. Geological Society, London, Special Publications, 231, pp. 73-87.

Price, N. J., Cosgrove, J. W., 1990. Analysis of geological structures, first ed. Cambridge University Press, Cambridge.

Priest, S. D., Hudson, J. A., 1976. Discontinuity spacings in rock. International Journal of Rock Mechanics & Mining Sciences 13, 135-148.

Pouya, A., Bemani Yazdi, P., 2015. A damage-plasticity model for cohesive fractures. International Journal of Rock Mechanics & Mining Sciences 73, 194-202.

Rabczuk, T., Bordas, S., Zi, G., 2010. On three-dimensional modelling of crack growth using partition of unity methods. Computers & Structures 88, 1391-1411.

Ramsay, J. G., 1967. Folding and fracturing of rocks, first ed. McGraw-Hill, New York.

Schlische, R. W., 1991. Half-graben basin filling models: new constraints on continental extensional basin development. Basin Research 3, 123-141.

Schultz-Ela, D. D., Jackson, M. P. A., Vendeville, B. C., 1993. Mechanics of active salt diapirism. Tectonophysics 228, 275-312.

Shi, G., Goodman, R. E., 1985. Two dimensional discontinuous deformation analysis. International Journal for Numerical and Analytical Methods in Geomechanics 9(6), 541-556.

Sukumar, N., Prévost, J.-H., 2003, Modeling quasi-static crack growth with the extended finite element method part I: computer implementation. International Journal of Solids and Structures 40, 7513-7537.

Swenson, D. V., Ingraffea, A. R., 1988. Modelling mixed-mode dynamic crack propagation using finite elements: theory and applications. Computational Mechanics 3, 381-397.

Tang, C. A., Liang, Z. Z., Zhang, Y. B., Chang, X., Tao, X., Wang, D. G., 2008. Fracture spacing in layered materials: a new explanation based on 2D failure process modeling. American Journal of Science 308, 49-72.

Wang, X., 2010. Modelling the evolution of fractures during layer normal compression of a limestone shale sequence using the combined FEMDEM numerical method, MSc thesis, Imperial College London.

Wu, H., Pollard, D. D., 1995. An experimental study of the relationship between joint spacing and layer thickness. Journal of Structural Geology 17(6), 887-905.

Xian, L., Bićanić, N., Owen, D. R. J., Munjiza, A., 1991. Rock blasting simulation by rigid body dynamics analysis and rigid brittle fracturing model, in: Bicanic, N. et al. (Eds.), Proceedings NEC-91, International Conference on Nonlinear Engineering Computations. Pineridge Press, Swansea, UK, pp. 577-587.

Xiang, J., Munjiza, A., Latham, J.-P., 2009. Finite strain, finite rotation quadratic tetrahedral element for the combined finite-discrete element method. International Journal for Numerical Methods in Engineering 79, 946-978.

Zoback, M. D., 2010. Reservoir geomechanics, first ed. Cambridge University Press, New York.